fluids

MDPI

Article

Modeling of Local Hematocrit for Blood Flow in Stenotic Coronary Vessels

Ilya Starodumov [1,2], Ksenia Makhaeva [1,3], Andrey Zubarev [1], Ivan Bessonov [4], Sergey Sokolov [1,2], Pavel Mikushin [1,5], Dmitri Alexandrov [3], Vasiliy Chestukhin [6] and Felix Blyakhman [1,2,*]

1 Laboratory of Multiphase Physical and Biological Media Modelling, Department of Theoretical and Mathematical Physics, Ural Federal University, Ekaterinburg 620000, Russia; ilya.starodumov@urfu.ru (I.S.); ksenia.makhaeva@urfu.ru (K.M.); a.j.zubarev@urfu.ru (A.Z.); sergey.sokolov@urfu.ru (S.S.); mikushin.pv18@physics.msu.ru (P.M.)
2 Department of Biomedical Physics and Engineering, Ural State Medical University, Ekaterinburg 620000, Russia
3 Laboratory of Multi-Scale Mathematical Modeling, Department of Theoretical and Mathematical Physics, Ural Federal University, Ekaterinburg 620000, Russia; dmitri.alexandrov@urfu.ru
4 Tyumen Cardiology Research Center, Tomsk National Research Medical Center, Russian Academy of Sciences, Tomsk 625026, Russia; bessonov@infarkta.net
5 Moscow Institute of Physics and Technology, Moscow 141701, Russia
6 Sklifosovsky Research Institute of Emergency Care, Moscow 129090, Russia; v.v.chestukhin@yandex.ru
* Correspondence: feliks.blyakhman@urfu.ru

Abstract: This mainly theoretical work is devoted to the study of the contribution of the cell-free layer (CFL) near the vessel wall to hemodynamics in a large coronary artery with stenosis to assess the relevance of CFL modeling to the needs of interventional cardiology. An Euler–Euler model considering blood as a two-component fluid with a discrete phase of erythrocytes and a liquid plasma phase was applied to a simple 2d vessel with 65% stenosis. It was found that both the CFL thickness and the local contribution of the CFL thickness to hemodynamics are inhomogeneous along the vessel. The effects of CFL on the velocity profiles, vortex formation, hematocrit, viscosity, and wall shear stresses in the area of stenosis were determined. To demonstrate the significance of CFL modeling for prognostic purposes, the same hemodynamic conditions, analyzed using a one-component model, were also considered. A comparison analysis showed that the existence of CFL resulted in a significant overestimation (up to over 100%) of the main hemodynamic characteristics of the flow obtained using the model based on the Carreau equation.

Keywords: hemodynamics; CFL; erythrocytes; multicomponent flow; computer modeling

Citation: Starodumov, I.; Makhaeva, K.; Zubarev, A.; Bessonov, I.; Sokolov, S.; Mikushin, P.; Alexandrov, D.; Chestukhin, V.; Blyakhman, F. Modeling of Local Hematocrit for Blood Flow in Stenotic Coronary Vessels. *Fluids* **2023**, *8*, 230. https://doi.org/10.3390/fluids8080230

Academic Editor: D. Andrew S. Rees

Received: 19 July 2023
Revised: 8 August 2023
Accepted: 15 August 2023
Published: 18 August 2023

1. Introduction

Cardiovascular diseases are among the main causes of death in the global population [1,2]. In most cases, the dysfunction of the myocardium, and the heart in general, is associated with the development of atherosclerosis in the coronary arteries of the cardiac wall. Atherosclerosis is a chronic focal lesion of the arteries that is accompanied by the formation of an atherosclerotic plaque on the vessel wall [3]. The plaque narrows the lumen of the vessel, leading to stenosis of the artery, which blocks normal blood flow.

Coronary artery stenosis is an important determinant of both local and systemic hemodynamics in the heart and of its function in general. Quantifying the contribution of stenosis to myocardial blood supply is a key task for physicians when choosing the right approach to patient treatment. In clinical practice, a number of non-invasive and minimally invasive diagnostic methods have been introduced to determine the geometry of stenosis, the velocity of blood flow through it, the pressure gradient before and after arterial narrowing, etc. The results of such instrumental observations form the basis of the mathematical and computer modeling of hemodynamics for prognostic purposes. The

development of this approach is a trend of modern medicine. Some advances in modeling have been applied in clinical practice [4,5].

The accuracy of the mathematical modeling of hemodynamic conditions in the heart critically depends on the set of parameters taken into account. In many studies of coronary hemodynamics, blood is mainly treated as a single-phase Newtonian or non-Newtonian fluid. Therefore, the effect of hematocrit (the volume fraction of erythrocytes in the blood) on flow characteristics has been neglected. However, the experimental data obtained by Cokelet [6] and the theoretical studies of Haynes [7] indicate that blood is not a single-phase liquid when moving through blood vessels with a diameter of up to 2400 microns. The same observation applies for large vessels [8]. Thus, a realistic description of blood flow, including in large coronary arteries, requires accounting for local hematocrit, considering erythrocytes as discrete particles [9].

In general, the particle theory field that describes the interaction between liquids and solids has been of great interest to scientists and engineers for more than two decades [10]. Concerning vascular hemodynamics, the effects of erythrocyte concentration and stenosis geometry on shear stress and flow resistance have been studied to some extent [11,12].

In the first half of the last century, two important phenomena of blood flow in arteries and capillaries were discovered. The first was a decrease in the average concentration of erythrocytes in narrow vessels, or the so-called Fahreus effect [13]. The second was a decrease in the effective viscosity in a blood vessel, or the so-called Fahreus–Lindquist effect [14]. Both of these effects are characterized by the formation of a cell-free layer (CFL) near the vascular wall. This layer of blood plasma separates the flow core from the walls of the vessel [15]. The CFL width is defined as the distance from the outer edge of the erythrocyte nucleus to the luminal surface of the endothelium, reflecting the dynamic position of the erythrocytes that are farthest from the flow core. Thus, the CFL phenomenon must be taken into account when modeling hemodynamics.

CFL modeling can be performed explicitly in multilayer vessel models, where the flow core thickness and CFL are selected or calculated. Each layer is a single-component continuous fluid with its own physical properties [16–18]. In this approach, one of the key issues remains the calculation of CFL thickness in vessels with a complex geometry and unsteady flows. Another implicit method is accounting for the cell-free layer, which involves modeling blood as a multicomponent medium including continuous plasma and dispersed erythrocytes and other particles. Euler–Euler or Euler–Lagrange mathematical approaches [19–21] can be used to model multiphase blood flow. As usual, in these approaches, blood plasma is modeled as a Newtonian fluid [22]. A multicomponent approach to the modeling of blood flow provides complete information on the properties and distribution of blood components.

The modeling of the cell-free layer in microcirculatory vessels has been extensively applied. In particular, it has been shown that CFL affects microcirculation, reduces local viscosity and flow resistance, and governs oxygen delivery and carbon dioxide removal [4,5]. At the same time, the contribution of CFL to the hemodynamics in macrocirculatory vessels is not yet clear. For example, in [18], where a two-layer continuum model with a constant CFL width was employed, the authors showed that CFL qualitatively and quantitatively contributes to the hemodynamics near stenosis. But in large vessels (like coronary arteries), the CFL width is variable and determined by a set of dynamic processes.

Presumably, parietal processes in large vessels may directly affect the formation of arterial occlusion and the results of patient treatment and rehabilitation. Therefore, the possible role of CFL in the development of these processes should be studied in detail.

The present study addresses the effects of CFL on the hemodynamics in a modeled macrocirculatory vessel like a brunch of the left coronary artery. An Euler–Euler model taking into account blood as a two-component fluid with the discrete phase of erythrocytes and the liquid phase of plasma is proposed. By employing a simple 2d vessel with 60% stenosis, we show the contribution of CFL to the velocity profiles, vortex formation, hematocrit, viscosity, and wall shear stresses in the area of stenosis. To demonstrate the significance of

the obtained results for practical use in coronary blood flow modeling in cardiology, we considered the same hemodynamic conditions using a one-component model based on the Carreau equation, which is widely used for the description of non-Newtonian blood properties. In accordance with a comparison of the results obtained using the two models, we show fundamental differences in the prognostic value of these simulations.

2. Materials and Methods

2.1. Two-Component Model of Blood: Equations Describing the Processes in the Dispersed Phase

The advection equation for the dispersed phase can be written as

$$\frac{\partial n}{\partial t} + \nabla \cdot (\boldsymbol{V}_d n) = 0. \tag{1}$$

Here, n $\left[\mathrm{m}^{-3}\right]$ is the concentration of the dispersed phase (i.e., the concentration of erythrocytes), and $\boldsymbol{V}_d$ $\left[\mathrm{m\ s}^{-1}\right]$ is the velocity of its motion.

The momentum transfer of the dispersed phase (erythrocytes) is described by the non-homogeneous convection equations for the conservative variables $\boldsymbol{V}_d$ and n:

$$\begin{aligned} & m_d \frac{\partial (\boldsymbol{V}_d n)}{\partial t} + m_d (n\boldsymbol{V}_d \cdot \nabla)\boldsymbol{V}_d = -n\frac{\pi d^3}{6}\nabla P + \boldsymbol{F}_D + \boldsymbol{F}_W, \\ & \boldsymbol{F}_D = n\rho_c C_D \frac{\pi d^2}{8}|\boldsymbol{V}_c - \boldsymbol{V}_d|(\boldsymbol{V}_c - \boldsymbol{V}_d), \\ & \boldsymbol{F}_W = n\rho_c C_W \frac{\pi d^3}{6} \max\left\{0, \left(\frac{1}{y} - \frac{1}{D_W}\right)\right\}(\boldsymbol{V}_c - \boldsymbol{V}_d)^2 \boldsymbol{N}. \end{aligned} \tag{2}$$

Here, m_d [kg] is the local mass of particles; d [m] is the particle diameter; P [Pa] is the fluid pressure measured relative to the hydrostatic pressure; ρ_c $\left[\mathrm{kg\ m}^{-3}\right]$ is the density of the continuous phase; $\boldsymbol{F}_D$ $\left[\mathrm{N\ m}^{-3}\right]$ is the drag force; C_D is the drag coefficient; $\boldsymbol{V}_c$ $\left[\mathrm{m\ s}^{-1}\right]$ is the velocity of the continuous phase; $\boldsymbol{F}_W$ $\left[\mathrm{N\ m}^{-3}\right]$ is the repulsive force (i.e., the force that repels the dispersed particles (erythrocytes) away from the wall); D_W [m] is the distance to the wall, at which point the action of the repulsive force stops; C_W is the repulsive force coefficient; y [m] is the distance from the particle center to the wall; and $\boldsymbol{N}$ is the normal direction in relation to the wall (directed towards the fluid).

To assess the drag coefficient of a particle cloud, the following expressions [23] are used:

$$C_D = \frac{24}{Re_d} + 0.44, \tag{3}$$

$$Re_d = \frac{\rho_c |\boldsymbol{V}_c - \boldsymbol{V}_d| d}{\mu_c}. \tag{4}$$

Here, Re_d is the Reynolds number for the dispersed phase, and μ_c is the molecular viscosity dynamic coefficient of the continuous phase $\left[\mathrm{kg\ m}^{-1}\ \mathrm{s}^{-1}\right]$.

2.2. Two-Component Model of Blood: Equations Describing the Processes in the Continuous Phase

The continuity equation can be written as

$$\rho_c \frac{\partial (\varphi_c)}{\partial t} + \nabla \cdot (\varphi_c \rho_c \boldsymbol{V}_c) = 0 \tag{5}$$

Here, φ_c is the relative volume of the continuous phase. The momentum equation assumes the following form:

$$\begin{aligned} &\frac{\partial(\varphi_c \rho_c \boldsymbol{V}_c)}{\partial t} + (\varphi_c \rho_c (\boldsymbol{V}_c \cdot \nabla)\boldsymbol{V}_c) = -\varphi_c \nabla p + \nabla \cdot (\varphi_c \boldsymbol{\tau}) - \boldsymbol{F}_D, \\ &\boldsymbol{\tau} = \mu_c 2\boldsymbol{S}, \\ &S_{ij} = \frac{1}{2}\left(\frac{\partial V_i}{\partial x_j} + \frac{\partial V_j}{\partial x_i}\right). \end{aligned} \tag{6}$$

Here, $\boldsymbol{\tau}$ [Pa] is the viscous stress tensor, μ_c $\left[\text{kg m}^{-1}\ \text{s}^{-1}\right]$ is the dynamic coefficient of molecular viscosity of the continuous phase, and $\boldsymbol{S}$ $\left[\text{s}^{-1}\right]$ denotes the absolute value of the generalized velocity gradient.

2.3. One-Component Continuous Model of Blood

For further analysis, we compare the two-component model with the more simple one-component model:

$$\begin{aligned} &\nabla \cdot \boldsymbol{V} = 0, \\ &\rho \tfrac{\partial \boldsymbol{V}}{\partial t} + \rho(\boldsymbol{V} \cdot \nabla)\boldsymbol{V} = -\nabla P + \nabla \cdot \boldsymbol{\tau_e}, \\ &\boldsymbol{\tau_e} = \mu(\hat{S}) 2\boldsymbol{S}, \\ &\hat{S} = 2\sum_{i,j} \hat{S}_{ij}^2,\ \hat{S}_{ij} = \tfrac{1}{2}\left(\frac{\partial V_i}{\partial x_j} + \frac{\partial V_j}{\partial x_i}\right). \end{aligned} \tag{7}$$

Here, **V** is the velocity vector, ρ is the constant density, P is pressure, $\boldsymbol{\tau_e}$ is the tensor of viscous stresses, μ is the coefficient of dynamic viscosity, and $\boldsymbol{I}$ represents the unit tensor.

Note that the main mechanism behind the nonlinearity of the blood state is the nonlinear dependence of the dynamic viscosity of the shear rate. Thus, blood can be considered a non-Newtonian fluid and described using various models [24]. In the current study, we consider the Carreau model [25], which has been successfully used for simulating blood flow in previous works [26,27]. This model can be expressed using the equation for dynamic viscosity μ:

$$\mu(\hat{S}) = \mu_{min} + (\mu_{max} - \mu_{min})\left(1 + \lambda^2 \hat{S}\right)^{\frac{n-1}{2}},\ \mu_{min} \le \mu \le \mu_{max}. \tag{8}$$

Here, μ_{min} and μ_{max} are the minimum and maximum viscosity values, respectively; n is the empirical constant; and λ is the relaxation coefficient of the form $\lambda = \sqrt{\frac{\mu_{max}}{\tau^*}}$, where τ^* stands for characteristic shear stress.

2.4. Design and Procedure of Simulations

Figure 1 presents a sketch of the computational domain used in the simulations.

In the case of a two-component model, the boundary condition on the left (see Figure 1 is normal with respect to the boundary $V_{c,in} = V_{d,in} = 0.5$ m/s for the fluid and erythrocyte velocity. Concentration n corresponds to a hematocrit value of 40%. The boundary conditions on the right follow the zero gradient condition for static pressure P and erythrocyte concentration n. We consider the upper boundary to be a rigid wall with a no-slip velocity effect. The lower limit corresponds to a rigid wall without a no-slip effect. This approach is

valid [26] and can be used for laminar flows in a straight axisymmetric channel. The shape of stenosis was determined using the expression

$$y(x) = \begin{cases} R\left[1 - G\left\{L_{st}(x-L) - (x-L)^2\right\}\right], & L \le x < L + L_{st} \\ R, & x < L \text{ or } x > L + L_{st} \\ G = \frac{\left(R^2 - y^2(x_{st})\right)}{R^2}, \end{cases} \quad (9)$$

and corresponds to a stenosis with an overlap of $G = 0.65$.

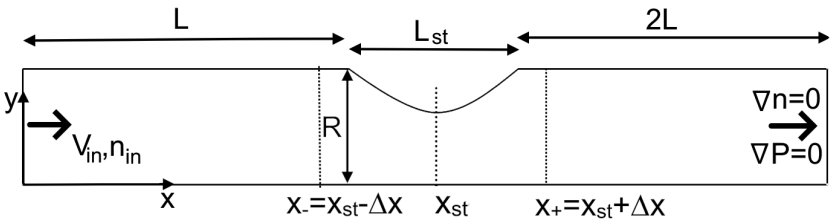

Figure 1. A sketch of the modeled vessel with stenosis. To ensure the symmetry of the solution, only half of the vessel is considered below. In our simulations, we consider $R = 1$ mm, $L = 8$ mm, $L_{st} = 3$ mm, and $\Delta x = 2$ mm.

Parameters for the two-component and one-component models are presented in Table 1.

Table 1. Parameters of the blood models.

Parameter	Value	Unit
ρ	1055	kg/m^3
n	0.3568	-
μ_{max}	0.056	Pa s
μ_{min}	0.004	Pa s
λ	3.131	s
ρ_c	1030	kg/m^3
μ_c	0.0013	Pa s
m_d	0.2	pkg
d	7	µm

To solve Equations (2)–(8), we used the finite-volume numerical scheme for a hexagonal mesh implemented in the FlowVision© CFD software [28]. Static adapted mesh thickening towards the wall was used to obtain the CFL solution in the vessel wall region. All computer simulations were executed on an HPC server with 2 × 64-core processors AMD EPYC 7763, 3.2 GHz (GIGABYTE TECHNOLOGY Co., Ltd., New Taipei City, Taiwan). Steady-state fluxes and erythrocyte concentrations were investigated; these fluxes were reached over a 24 h computational time period. Test calculations were executed to investigate mesh convergence and the number of hexogonal cells. The calculations were performed for a two-component model, and the parameters of mean dynamic pressure and mean velocity were investigated; the results, presented in Figure 2, show that 108,000 cells is an optimal amount for the mesh. The mesh size in the flow core did not exceed 20 µm. In the region of assumed CFL, the cell size did not exceed 5 µm (see Figure 2). In Figure 1, $x_{st} - \Delta x$, x_{st}, $x_{st} + \Delta x$ points in the stenosis area are noted, and they are used in the next sections for a detailed analysis of steady hemodynamic flow properties.

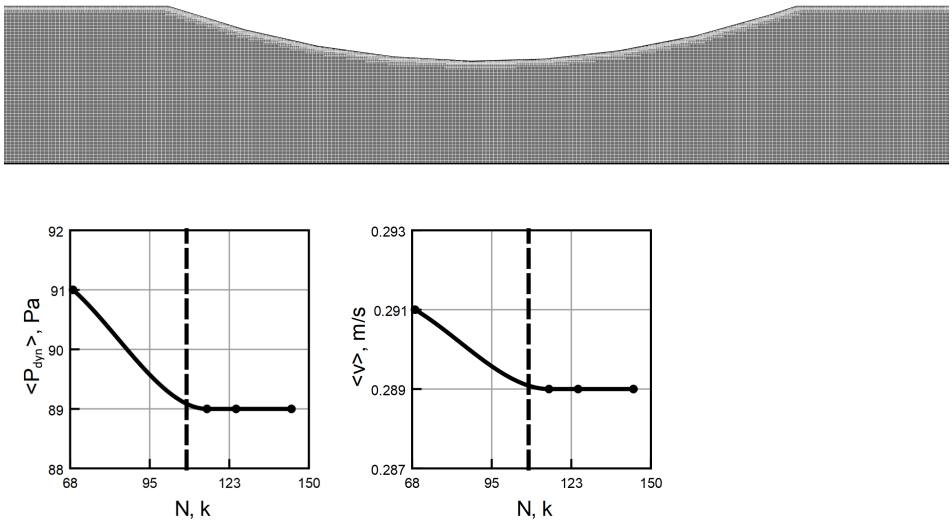

Figure 2. Upper panel: computational grid after adaptation in near-wall region. **Lower panel**: dependence of the mean dynamic pressure <P_{dyn}> and mean velocity <v> on the number of cells in the computational grid N for the two-component model. The dashed line corresponds to N = 108,000 cells.

3. Results

The simulations investigated the hemodynamic flow characteristics of a one-component model with viscosity determined by the Carreau equation as well as a two-component model with an additional particle-wall repulsion force F_W scaled by the factor C_W. We consider the case $C_W = 0$, corresponding to the two-component model with no F_W force, and the case $C_W = 0.9$, which, as we will see, yields a CFL with a layer thickness consistent with known experimental work. The two-component model results will be compared with the results of the one-component model with reference to the parameters in Table 1.

Figures 3 and 4 show the volume fraction of erythrocytes in the vessel corresponding to the two-component model with $C_W = 0$ and $C_W = 0.9$. We can see that at the scales of the vessel radius in both cases, the distributions of hematocrit are similar and close to uniform. A difference is observed in the near-wall region of the vessel with a width of about 15 μm, where, in the presence of the repulsive force of erythrocytes from the vessel wall, the volume fraction of erythrocytes falls sharply, leading to the formation of the CFL zone before stenosis (see Figure 4a). If there is no repulsive force, the volume fraction of erythrocytes remains unchanged, and no CFL is formed.

Inside the stenosis (Figure 4b), a pressure drop and flow acceleration lead to the thinning of the CFL and even its complete disappearance. Thus, the results of modeling with $F_W = 0$ and in the presence of this force are similar.

However, after stenosis (Figure 4c), the conditions for CFL formation reappear in the low-velocity recirculation zone. Moreover, since the convective flows in this region are very weak, the CFL becomes more distinct and stable.

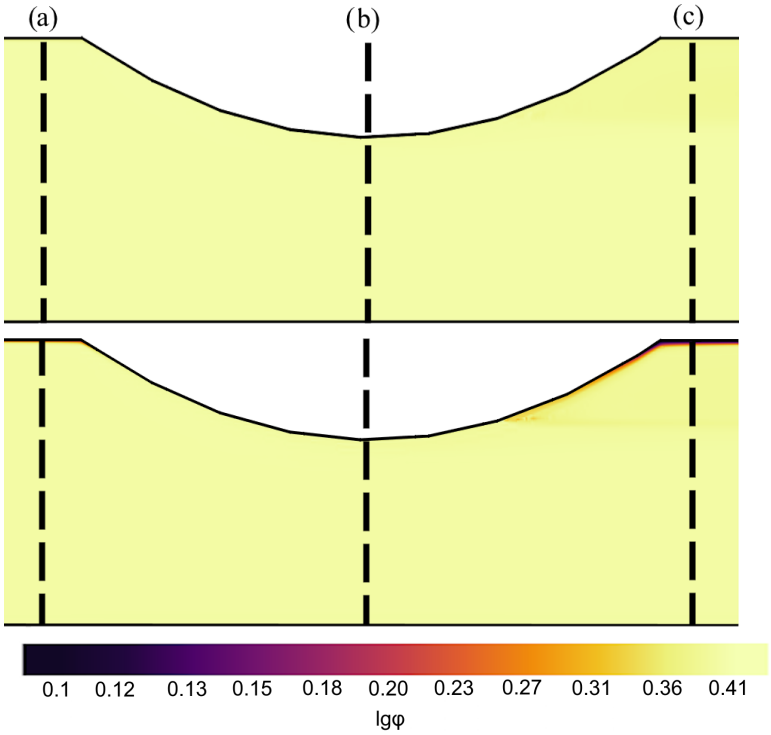

Figure 3. Distribution of erythrocyte volume fraction $\varphi = \frac{\pi d^3}{6} n$ in the area of stenosis. **Upper panel**: two-component model with $C_W = 0$; **lower panel**: two-component model with $C_W = 0.9$. Panels correspond to cross-sections for x-coordinate: (**a**) $x_{st} - \Delta x$, (**b**) x_{st}, and (**c**) $x_{st} + \Delta x$ (see Figure 1). Profiles for the corresponding cross-sections (**a**–**c**) are presented in (Figure 4). Figures are compressed along the horizontal axis for demonstrative purposes.

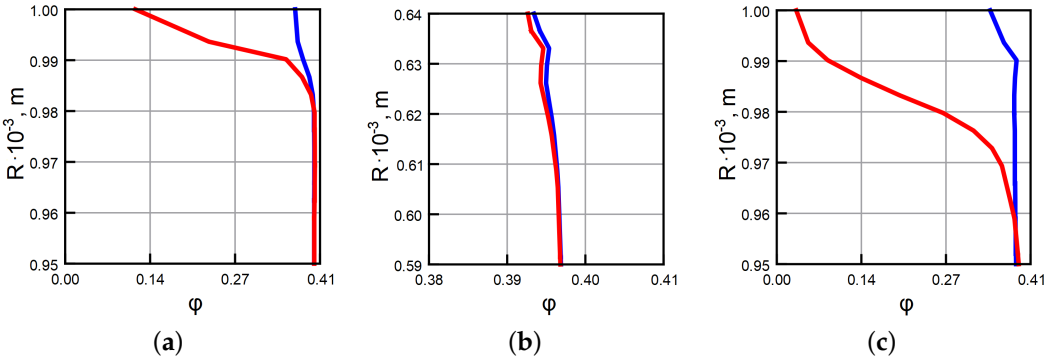

Figure 4. Dependence of erythrocyte volume fraction φ on the distance to the vessel wall. Blue line—two-component model with $C_W = 0$; red line—two-component model with $C_W = 0.9$. Panels correspond to cross-sections for x-coordinate: (**a**) $x_{st} - \Delta x$, (**b**) x_{st}, (**c**) $x_{st} + \Delta x$ (see Figure 1).

The formation of an inhomogeneous CFL along the vessel affects the viscosity of the near-wall layer, which can decrease to several times lower than the plasma viscosity value.

The effective viscosity for the two-component medium can be calculated [29] using Einstein's equation

$$\mu = \mu_c(1 + A\varphi), \tag{10}$$

where φ is the volume fraction of erythrocytes, A is the parameter corresponding to the ratio of semi-axes of the ellipsoid particle, and μ_c is the dynamic viscosity of plasma. For a healthy erythrocyte, the sizes of the semiaxes can be assumed to be [30] $a = 8.5$ µm, $b = 2.4$ µm, which yields $A = 6$ [29].

Figure 5 and 6 shows the differences in effective viscosity for the one-component and two-component models. We can see that in the sections before and after the stenosis

(Figure 5a,c), where a CFL is formed, in the near-wall region, the two-component model yields a significantly less viscous plasma viscosity than that in the flow core. The one-component model cannot predict such a drop in viscosity because this effect is caused by a local change in hematocrit. On the other hand, the one-component model describes in detail the changes in viscosity outside the CFL caused by the effects of aggregation, cell deformation, and other processes empirically described by the Carreau equation.

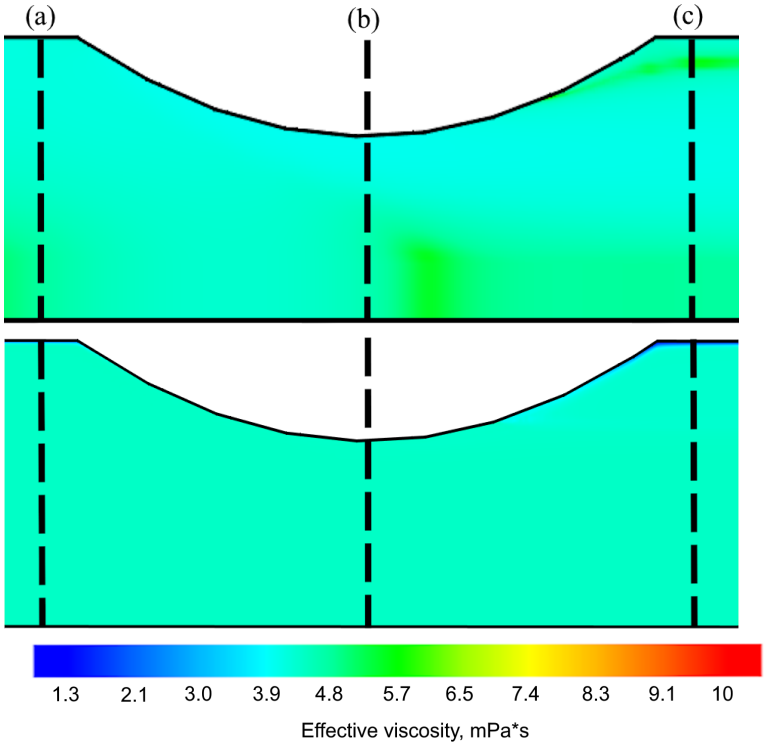

Figure 5. Distribution of effective viscosity μ in the area of stenosis. **Upper panel**: one-component Carreau model; **lower panel**: two-component model with $C_W = 0.9$. Panels correspond to cross-sections for x-coordinate: (**a**) $x_{st} - \Delta x$, (**b**) x_{st}, and (**c**) $x_{st} + \Delta x$ (see Figure 1). Profiles for the corresponding cross-sections (**a**–**c**) are presented in this figure.

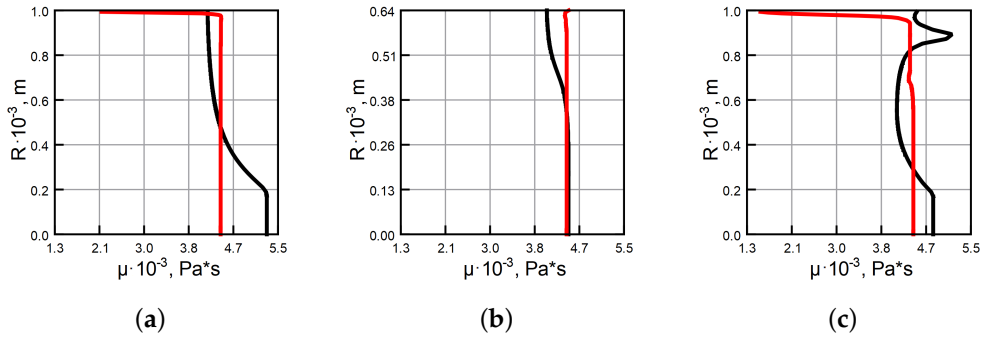

Figure 6. Dependence of effective viscosity μ on the distance to the vessel wall. Black line—one-component Carreau model; red line—two-component model with $C_W = 0.9$. Panels correspond to cross-sections for x-coordinate: (**a**) $x_{st} - \Delta x$, (**b**) x_{st}, and (**c**) $x_{st} + \Delta x$ (see Figure 1).

With such a significant difference in local viscosity, the formation of a two-component, reduced-viscosity CFL model naturally precipitates changes in the cross-sectional velocity profiles and in the features of the recirculation region behind the stenosis.

Figure 7 shows the size and shape of the vortex in the case of the one-component model and the two-component model. The appearance of a CFL in the second case stretched

the vortex zone several times. In addition, it can be seen that the two-component model is characterized by less convex velocity profiles (Figure 8).

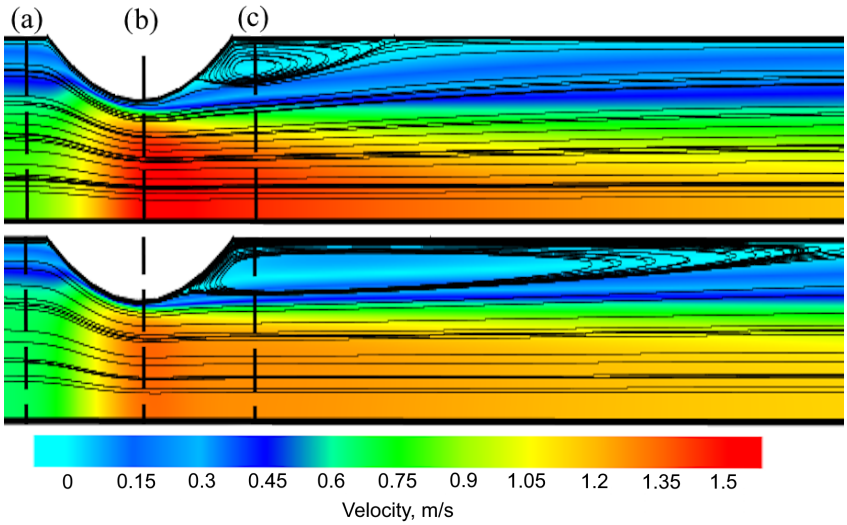

Figure 7. Recirculation regions after stenosis. **Upper panel**: one-component Carreau model; **lower panel**: two-component model with $C_W = 0.9$. Figures are compressed along the horizontal axis for demonstrative purposes. Profiles for the corresponding cross-sections (**a**–**c**) are presented in (Figure 8).

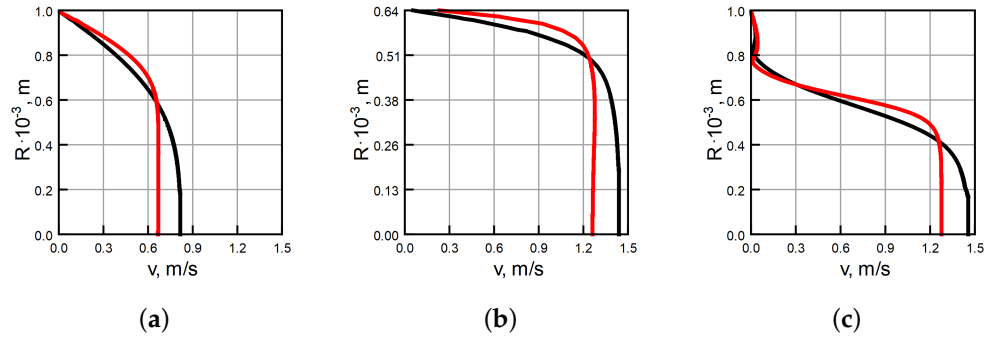

Figure 8. Velocity profiles for different cross-sections. Black line—one-component Carreau model; red line—two-component model with $C_W = 0.9$. Panels correspond to cross-sections for x-coordinate: (**a**) $x_{st} - \Delta x$, (**b**) x_{st}, and (**c**) $x_{st} + \Delta x$ (see Figure 1).

Figure 9 shows the pressure profiles. It can be seen that for the two-component model, the pressure in the flow core is almost 100% higher than that for the one-component model. At the same time, by taking into account the CFL, near the wall, the pressure drops and becomes almost 50% lower than that in the case of the one-component model. The greatest difference in the pressure profiles is observed in the interior of the stenosis and in the recirculation region (see Figure 9b,c).

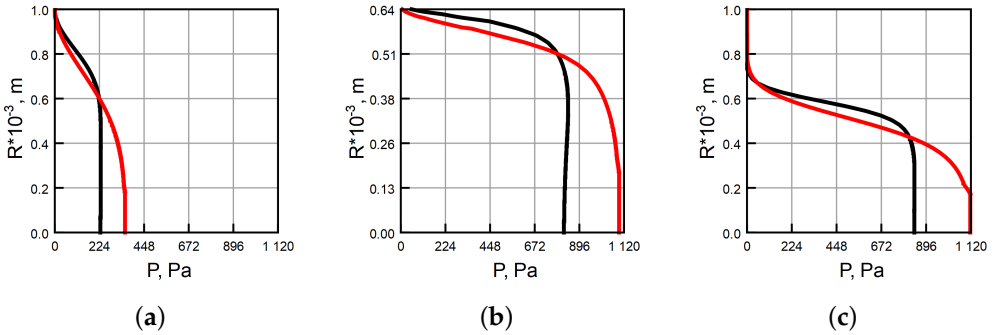

Figure 9. Pressure profiles for different cross-sections. Black line—one-component Carreau model; red line—two-component model with $C_W = 0.9$. Panels correspond to cross-sections for x-coordinate: (**a**) $x_{st} - \Delta x$, (**b**) x_{st}, and (**c**) $x_{st} + \Delta x$ (see Figure 1).

In addition, the wall shear stresses were calculated for the investigated segments. The results are presented in Table 2. We can see that even without the force of erythrocyte repulsion from the wall, the shear stress in the two-component model is three times lower than in the one-component Carreau model. The appearance of a CFL due to the repulsive force decreases the shear stress of the wall even further. This effect is less noticeable in the stenosis itself because the CFL formation is less pronounced, but before and after stenosis, the effect is very significant.

Table 2. Calculated wall shear stress for the region near stenosis. Two-component model ($C_W = 0$; $C_W = 0.9$) and one-component Carreau model comparison.

Cross-Section	$C_W = 0$	$C_W = 0.9$	Carreau
$x_{st} - \Delta x$	2.33	1.50	6.03
x_{st}	26.06	25.17	38.04
$x_{st} + \Delta x$	0.82	0.58	2.78

4. Discussion

The CFL is a widely studied phenomenon due to its fundamental importance (e.g., [31–33]). In particular, the CFL plays a major role in maintaining hemostasis and the body's immune response (e.g., as reported in [34,35]). The CFL determines wall shear stress, which is perceived by endothelial cells and triggers various pathophysiological functions (e.g., [36–38]). In addition, CFLs provide a barrier that inhibits the consumption of nitric oxide (NO), a vasodilator produced in the vascular endothelium (e.g., [39,40]). Nitric oxide plays an important role in preventing atherosclerosis [41] and thrombosis [42]. The altered transport of NO induces atherogenesis [43]. Furthermore, the thickness of a CFL is directly related to the phenomenon of plasma skimming, which contributes to the heterogeneous distribution of hematocrit across daughter branches during vessel bifurcation [44].

All relevant information on the nature of the cell-free layer has been obtained from in vitro studies [45,46]. In terms of theoretical applications, a number of low-dimensional models of microvascular blood flow use CFL thickness as an input parameter (e.g., [18,47]). The feasibility of non-empirical in silico modeling and the applicability of these data to in vivo situations are still unclear.

A myocardial infarction is the main complication of coronary atherosclerosis development, and it is accompanied by a rupture or erosion of the atherosclerotic plaque cover [48]. The morphological features of plaques caused by atherosclerosis have been well studied using intravascular imaging techniques [49,50]. In particular, a high risk of vascular accidents is associated with "vulnerable atherosclerotic plaques", which are characterized by a thinned fibrous cap and a large area of the necrotic core [51]. A number of factors

govern the growth and development of atherosclerotic plaque instability. Among them, the peculiarities of local hemodynamics may play a key role in this process [52–57].

Since the existence of the CFL has important hemorheologic and physiologic implications in both healthy and diseased states [34–43], the effects of the CFL on the hemodynamics in a modeled macrocirculatory vessel with stenosis were the focus of the present study.

There is a considerable amount of information on the dependence of CFL thickness on vessel diameter, hematocrit, flow and shear rates, and other relevant values. Generally, these studies show that thickness increases with decreasing hematocrit and increasing flow rate and vessel diameter [15]. In long, straight vessels, a number of competing hydrodynamic mechanisms can be identified that play a role in CFL formation [58]. Under normal conditions, healthy erythrocytes are highly elastic. Their deformability leads to the migration of erythrocytes away from vessel walls and from regions with a large velocity gradient to a smaller region [59,60]. Healthy erythrocytes experience tank-treading motion at weak to moderate shear flows near a vessel wall. As a result, erythrocytes experience a lifting force near the vessel wall, which causes them to drift away from the wall [61]. Some studies allow for the modification of multicomponent models to simulate the behavior and deformation of "healthy" and "diseased" erythrocytes [62]. The deformability of erythrocytes has also been studied [63].

In our investigation, the developed two-component model reproduced this phenomenon by explicitly accounting for the distribution of local erythrocyte concentrations and using F_W force in the momentum Equation (2). F_W force, determined by a combination of shear or other relevant forces (dispersive or aggregation) acting on the cell surface, changes over time due to hemodynamic processes in plasma. This leads to temporal changes and an asymmetric structure of the CFL with respect to the vessel axis.

The one-component model assumes that fluid is homogeneous outside of CFLs; therefore, the values of viscosity and wall shear stress are significantly overestimated in the near-wall regions. This leads to both the distortion of the hemodynamic picture as a whole (changes in the profile of flow velocity, size, and the shape of the recirculation zone after stenosis) and an alternative interpretation of the results from the medical point of view.

These data allow us to conclude that the CFL cannot be considered a universal parameter for a wide class of vessels: the shape of the vessel and the parameters of the medium can increase or decrease the thickness of the CFL several times. At the same time, as shown in the present paper, these microscopic changes in the CFL will significantly affect the macroscopic processes in the vessel. Even for a symmetric vessel with an analytically defined geometry, the CFL cannot be predicted in advance. For this reason, the use of two- and multilayer models with a specified constant CFL thickness cannot be considered a reliable method for analyzing hemodynamic flows in real vessels with complex shapes. In addition, practical hemodynamic modeling is often associated with the study of blood–wall interactions, but even simple characteristics of such interactions (e.g., wall shear stress) change significantly in the presence of a CFL.

For example, a recent paper [18] proposed a two-layer model of hemodynamics in an ideal artery with stenoses of different shapes. It can be seen that, qualitatively, the results and conclusions of that paper correspond to the findings presented in our study: the existence of a CFL reduces the flow velocity in the center of a vessel and decreases wall shear stress and the plug core radius. However, the implicit two-layer model is only applicable to stationary problems, which means that it is impossible to study pulsating blood flow in a vessel. In addition, this model cannot predict the variability in CFL thickness in the axial direction, which, as shown in Figure 3, can be observed near stenosis: the CFL thickness in the present work using two-component model varies from 10 μm to over 30 μm. Variable CFL thickness leads to great local deviations in effective viscosity (see Figure 5; spread up to 200%), wall shear stress (see Table 2; spread up to 300%), local velocity, and pressure (see Figures 8 and 9; spread up to 20%), which are of fundamental importance in the study of medical applications.

The solution in this regard may be the use of two-component explicit models, where erythrocytes are a separate, dispersed phase that interacts with the carrier continuous phase, i.e., plasma. However, such models are much more computationally intensive than implicit ones, especially for large vessels, as they must be solved at micron resolution. In complex practical problems taking into account the deformation of large arterial walls (so-called fluid–solid interaction problems) and unsteady three-dimensional flows, the explicit calculation of CFLs becomes an excessively difficult problem. Therefore, combining two-layer implicit models with a dynamic CFL thickness function seems most promising. The compilation of such a function can be performed empirically using the explicit model from the current paper.

The proposed approach has a number of general limitations. We consider the vessel as a tube with rigid smooth walls; however, in a real large vessel, the vibrations and deformation of the walls have a significant influence. To take this into account, it is necessary to consider a fluid–solid interaction (FSI) problem that takes into account the elasticity of vessel tissues. In addition to axial flux in a vessel, there are also transverse fluxes from the walls, which change the entire configuration of local blood flow. In this case, the CFL becomes an unstable non-stationary region whose influence on hemodynamic indicators is very difficult to predict. Also, for large vessels, the effect of local turbulization of blood flow is important. This effect, together with wall oscillation, can lead to complex vortex formation in the vessel. The modeling of such cases is computationally complex and requires clinical data of high quality. Another serious limitation is related to the boundary conditions at the entrance to and exit from the vessel. For the steady-state case, constant boundary conditions corresponding to blood flow velocities in large human arteries were used in this paper. In earlier works [27,64], it was noted that unsteady boundary conditions play a crucial role in the formation of the flow inside a vessel and the transport of dispersed particles.

It should be noted that, in general, multiphase models are computationally complex and require high-performance hardware and software. Therefore, in addition to theoretical limitations, the considered approach has a technical limitation, i.e.,the required computational time.

5. Conclusions

A two-component model for describing blood flow in a straight vessel with stenosis was considered and compared with a widely used one-component rheological model in which Carreau's formula is used to describe viscosity. The two-component model represents a carrying continuous fluid (blood plasma) and a dispersed admixture at a ratio of 40% by volume (erythrocytes). The model is also augmented with the repulsive force of erythrocytes from the vessel wall, the magnitude of which is controlled by a selectable coefficient. This force allows us to scrutinize the cell-free layer (CFL), whose existence has been shown in many in vitro studies. Computer simulations were performed for conditions typical for human coronary vessels, which allowed us to compare both the macroscopic hemodynamic situation (velocity profiles and vortex formation) and microscopic characteristics on the CFL scale (local hematocrit, viscosity, and wall shear stresses). The comparison of the results obtained with the two-component model and the simulations carried out using the one-component model showed a significant quantitative and qualitative difference, the main reason for which was the CFL. Indeed, the CFL has a significantly lower viscosity than the bulk of blood because the CFL mainly consists of plasma. This low-viscosity wall layer acts as a lubricant for the main flow, which fundamentally changes the corresponding hemodynamics. Simple one-component models do not account for the local hematocrit, and therefore, cannot reproduce the CFL and overestimate the viscosity near the wall, which can be justified only for highly curved sections of vessels or swirling flows, where the erythrocyte concentrations are almost uniform across the cross-section of the vessel and the thickness of the CFL is very tiny.

Additionally, it has been shown that the process of CFL formation is inhomogeneous along the vessel and is unsteady over time. This phenomenon is explained by the fact that CFL thickness is influenced by a combination of variable forces and effects, such as the hydrodynamic force of interaction between erythrocytes and plasma; repulsion forces from the wall, including the effects of cell deformation and their elastic interaction with each other; and so on. Thus, for real three-dimensional vessels with unsteady blood pulsations, the proposed model that explicitly accounts for the local hematocrit significantly exceeds the previously proposed two- and multilayer stationary rheological models, in which CFL thickness is assumed to be homogeneous along the vessel. The error in CFL calculation can be more than 100%, which leads to a significant overestimation of the key hemodynamic properties of flow, namely, velocity, pressure, wall shear stress, and viscosity. In addition, local blood properties affect global hemodynamic patterns, such as the vortex zone behind the stenosis.

At the same time, for large vessels (such as coronary arteries), the contribution of microscale processes associated with CFLs may be crucial in modeling macrocharacteristics such as fractional flow reserve (FFR), resistivity, the formation of recirculation vortexes, and the accumulation of blood cells and fibrinogens therein. In addition, the CFL is directly related to gas exchange and the nutrition of the vessel epithelium, which are critical in the study of plaque growth and vascular pathologies.

Author Contributions: Conceptualization, I.S. and F.B.; methodology, I.S. and K.M.; software, K.M. and S.S.; formal analysis, F.B. and D.A.; investigation, I.S., V.C., F.B. and K.M.; resources, I.B.; data curation, I.B. and S.S.; writing—original draft preparation, I.S., F.B., K.M., I.B., P.M. and S.S.; writing—review and editing, I.S., F.B., P.M., S.S. and V.C.; visualization, I.S. and K.M.; supervision, I.S., A.Z. and F.B.; project administration, I.S. and F.B.; funding acquisition, I.S. and F.B. All authors have read and agreed to the published version of the manuscript.

Funding: This study was supported by the Russian Science Foundation (project no. 22-71-10071).

Data Availability Statement: Data is contained within the article.

Conflicts of Interest: The authors declare no conflict of interest.

References

1. Mensah, G.A.; Roth, G.A.; Fuster, V. The global burden of cardiovascular diseases and risk factors: 2020 and beyond. *J. Am. Coll. Cardiol.* **2019**, *74*, 2529–2532. [CrossRef]
2. Timmis, A.; Vardas, P.; Townsend, N.; Torbica, A.; Katus, H.; De Smedt, D.; Gale, C.P.; Maggioni, A.P.; Petersen, S.E.; Huculeci, R.; et al. European Society of Cardiology: Cardiovascular disease statistics 2021. *Eur. Heart J.* **2022**, *43*, 716–799. [CrossRef] [PubMed]
3. Libby, P.; Buring, J.; Badimon, L.; Hansson, G.; Deanfield, J.; Bittencourt, M.; Tokgözoğlu, L.; Lewis, E.F. Atherosclerosis. *Nat. Rev. Dis. Prim.* **2019**, *5*, 56. [CrossRef]
4. Namgung, B.; Liang, L.H.; Kim, S. Physiological significance of cell-free layer and experimental determination of its width in microcirculatory vessels. In *Visualization and Simulation of Complex Flows in Biomedical Engineering*; Springer: Dordrecht, The Netherlands, 2014; pp. 75–87.
5. Baskurt, O.K.; Meiselman, H.J. Blood rheology and hemodynamics. *Semin. Thromb. Hemost.* **2003**, *29*, 435–450.
6. Cokelet, G.R. The Rheology of Human Blood. Ph.D. Thesis, Massachusetts Institute of Technology, Cambridge, MA, USA, 1963.
7. Haynes, R.H. Physical basis of the dependence of blood viscosity on tube radius. *Am. J. Physiol.-Leg. Content* **1960**, *198*, 1193–1200. [CrossRef] [PubMed]
8. Srivastava, L.; Srivastava, V. On two-phase model of pulsatile blood flow with entrance effects. *Biorheology* **1983**, *20*, 761–777. [CrossRef] [PubMed]
9. Ademiloye, A.; Zhang, L.; Liew, K. Numerical computation of the elastic and mechanical properties of red blood cell membrane using the higher-order Cauchy–Born rule. *Appl. Math. Comput.* **2015**, *268*, 334–353. [CrossRef]
10. Gad, N. Effect of Hall currents on interaction of pulsatile and peristaltic transport induced flows of a particle–fluid suspension. *Appl. Math. Comput.* **2011**, *217*, 4313–4320. [CrossRef]
11. Srivastava, V. Particulate suspension blood flow through stenotic arteries: Effects of hematocrit and stenosis shape. *Indian J. Pure Appl. Math.* **2002**, *33*, 1353–1360.
12. Mekheimer, K.S.; Kot, M.A.E. Suspension model for blood flow through arterial catheterization. *Chem. Eng. Commun.* **2010**, *197*, 1195–1214. [CrossRef]
13. Fåhraeus, R. The suspension stability of the blood. *Physiol. Rev.* **1929**, *9*, 241–274. [CrossRef]

14. Fåhræus, R.; Lindqvist, T. The viscosity of the blood in narrow capillary tubes. *Am. J. Physiol.-Leg. Content* **1931**, *96*, 562–568. [CrossRef]
15. Kim, S.; Ong, P.K.; Yalcin, O.; Intaglietta, M.; Johnson, P.C. The cell-free layer in microvascular blood flow. *Biorheology* **2009**, *46*, 181–189. [CrossRef]
16. Srivastava, V.; Saxena, M. Two-layered model of Casson fluid flow through stenotic blood vessels: Applications to the cardiovascular system. *J. Biomech.* **1994**, *27*, 921–928. [CrossRef]
17. Haldar, K.; Andersson, H. Two-layered model of blood flow through stenosed arteries. *Acta Mech.* **1996**, *117*, 221–228. [CrossRef]
18. Ponalagusamy, R.; Manchi, R. A study on two-layered (K.L-Newtonian) model of blood flow in an artery with six types of mild stenoses. *Appl. Math. Comput.* **2020**, *367*, 124767. [CrossRef]
19. Melka, B.; Adamczyk, W.P.; Rojczyk, M.; Nowak, M.L.; Gracka, M.; Nowak, A.J.; Golda, A.; Bialecki, R.A.; Ostrowski, Z. Numerical investigation of multiphase blood flow coupled with lumped parameter model of outflow. *Int. J. Numer. Methods Heat Fluid Flow* **2019**, *30*, 228–244. [CrossRef]
20. Aryan, H.; Beigzadeh, B.; Siavashi, M. Euler-Lagrange numerical simulation of improved magnetic drug delivery in a three-dimensional CT-based carotid artery bifurcation. *Comput. Methods Programs Biomed.* **2022**, *219*, 106778. [CrossRef] [PubMed]
21. Gracka, M.; Lima, R.; Miranda, J.M.; Student, S.; Melka, B.; Ostrowski, Z. Red blood cells tracking and cell-free layer formation in a microchannel with hyperbolic contraction: A CFD model validation. *Comput. Methods Programs Biomed.* **2022**, *226*, 107117. [CrossRef] [PubMed]
22. Kim, J.; Antaki, J.F.; Massoudi, M. Computational study of blood flow in microchannels. *J. Comput. Appl. Math.* **2016**, *292*, 174–187. [CrossRef]
23. James, P.; Hewitt, G.; Whalley, P. *Droplet Motion in Two-Phase Flow*; Technical Report; Atomic Energy Authority Research Establishment: Harwell, UK, 1980.
24. Wajihah, S.A.; Sankar, D. A review on non-Newtonian fluid models for multi-layered blood rheology in constricted arteries. *Arch. Appl. Mech.* **2023**, *93*, 1771–1796. [CrossRef] [PubMed]
25. Carreau, P.J. Rheological equations from molecular network theories. *Trans. Soc. Rheol.* **1972**, *16*, 99–127. [CrossRef]
26. Starodumov, I.O.; Blyakhman, F.A.; Sokolov, S.Y.; Bessonov, I.S.; Zubarev, A.Y.; Alexandrov, D.V. In-silico study of hemodynamic effects in a coronary artery with stenosis. *Eur. Phys. J. Spec. Top.* **2020**, *229*, 3009–3020. [CrossRef]
27. Starodumov, I.O.; Sokolov, S.Y.; Alexandrov, D.V.; Zubarev, A.Y.; Bessonov, I.S.; Chestukhin, V.V.; Blyakhman, F.A. Modelling of hemodynamics in bifurcation lesions of coronary arteries before and after myocardial revascularization. *Philos. Trans. R. Soc. A* **2022**, *380*, 20200303. [CrossRef] [PubMed]
28. Aksenov, A.A. Flowvision: Industrial computational fluid dynamics. *Comput. Res. Model.* **2017**, *9*, 5–20. [CrossRef]
29. Landau, L.D.; Lifshitz, E.M. *Fluid Mechanics: Landau and Lifshitz: Course of Theoretical Physics*; Elsevier: Amsterdam, The Netherlands, 2013; Volume 6.
30. Gurevich, M.; Bernshtein, S. *Osnovy Gidrodinamiki*; Naukova Dumka: Kiev, USSR, 1979. (In Russian)
31. Fedosov, D.A.; Caswell, B.; Popel, A.S.; Karniadakis, G.E. Blood flow and cell-free layer in microvessels: Blood flow and cell-free layer in microvessels. *Microcirculation* **2010**, *17*, 615–628. [CrossRef]
32. Yin, X.; Thomas, T.; Zhang, J. Multiple red blood cell flows through microvascular bifurcations: Cell free layer, cell trajectory, and hematocrit separation. *Microvasc. Res.* **2013**, *89*, 47–56. [CrossRef]
33. Namgung, B.; Ong, P.K.; Johnson, P.C.; Kim, S. Effect of cell-free layer variation on arteriolar wall shear stress. *Ann. Biomed. Eng.* **2011**, *39*, 359–366. [CrossRef] [PubMed]
34. Freund, J.B. Leukocyte margination in a model microvessel. *Phys. Fluids* **2007**, *19*, 023301. [CrossRef]
35. Fedosov, D.A.; Gompper, G. White blood cell margination in microcirculation. *Soft Matter* **2014**, *10*, 2961–2970. [CrossRef]
36. Smiesko, V.; Johnson, P. The arterial lumen is controlled by flow-related shear stress. *Physiology* **1993**, *8*, 34–38. [CrossRef]
37. Davies, P.F.; Tripathi, S.C. Mechanical stress mechanisms and the cell. An endothelial paradigm. *Circ. Res.* **1993**, *72*, 239–245. [CrossRef]
38. Barbee, K.A. Role of subcellular shear–stress distributions in endothelial cell mechanotransduction. *Ann. Biomed. Eng.* **2002**, *30*, 472–482. [CrossRef] [PubMed]
39. Rees, D.D.; Palmer, R.M.; Moncada, S. Role of endothelium-derived nitric oxide in the regulation of blood pressure. *Proc. Natl. Acad. Sci. USA* **1989**, *86*, 3375–3378. [CrossRef]
40. Liao, J.C.; W. Hein, T.; Vaughn, M.W.; Huang, K.T.; Kuo, L. Intravascular flow decreases erythrocyte consumption of nitric oxide. *Proc. Natl. Acad. Sci. USA* **1999**, *96*, 8757–8761. [CrossRef] [PubMed]
41. Sarkar, R.; Meinberg, E.G.; Stanley, J.C.; Gordon, D.; Clinton Webb, R. Nitric oxide reversibly inhibits the migration of cultured vascular smooth muscle cells. *Circ. Res.* **1996**, *78*, 225–230. [CrossRef]
42. Radomski, M.; Palmer, R.; Moncada, S. The anti-aggregating properties of vascular endothelium: Interactions between prostacyclin and nitric oxide. *Br. J. Pharmacol.* **1987**, *92*, 639–646. [CrossRef]
43. Liu, X.; Fan, Y.; Xu, X.Y.; Deng, X. Nitric oxide transport in an axisymmetric stenosis. *J. R. Soc. Interface* **2012**, *9*, 2468–2478. [CrossRef]
44. Enden, G.; Popel, A.S. A numerical study of plasma skimming in small vascular bifurcations. *J. Biomech. Eng.* **1994**, *116*, 79–88. [CrossRef] [PubMed]

45. Yaginuma, T.; Oliveira, M.S.N.; Lima, R.; Ishikawa, T.; Yamaguchi, T. Human red blood cell behavior under homogeneous extensional flow in a hyperbolic-shaped microchannel. *Biomicrofluidics* **2013**, *7*, 054110. [CrossRef]
46. Rodrigues, R.O.; Lopes, R.; Pinho, D.; Pereira, A.I.; Garcia, V.; Gassmann, S.; Sousa, P.C.; Lima, R. In vitro blood flow and cell-free layer in hyperbolic microchannels: Visualizations and measurements. *BioChip J.* **2016**, *10*, 9–15. [CrossRef]
47. Perkkiö, J.; Keskinen, R. Hematocrit reduction in bifurcations due to plasma skimming. *Bull. Math. Biol.* **1983**, *45*, 41–50. [CrossRef]
48. Palasubramaniam, J.; Wang, X.; Peter, K. Myocardial infarction—From atherosclerosis to thrombosis: Uncovering new diagnostic and therapeutic approaches. *Arterioscler. Thromb. Vasc. Biol.* **2019**, *39*, e176–e185. [CrossRef]
49. Ali, Z.A.; Karimi Galougahi, K.; Mintz, G.S.; Maehara, A.; Shlofmitz, R.A.; Mattesini, A. Intracoronary optical coherence tomography: State of the art and future directions. *EuroIntervention* **2021**, *17*, e105–e123. [CrossRef] [PubMed]
50. Malaiapan, Y.; Leung, M.; White, A.J. The role of intravascular ultrasound in percutaneous coronary intervention of complex coronary lesions. *Cardiovasc. Diagn. Ther.* **2020**, *10*, 1371. [CrossRef]
51. Arbab-Zadeh, A.; Fuster, V. From detecting the vulnerable plaque to managing the vulnerable patient: JACC state-of-the-art review. *J. Am. Coll. Cardiol.* **2019**, *74*, 1582–1593. [CrossRef] [PubMed]
52. Zhou, M.; Yu, Y.; Chen, R.; Liu, X.; Hu, Y.; Ma, Z.; Gao, L.; Jian, W.; Wang, L. Wall shear stress and its role in atherosclerosis. *Front. Cardiovasc. Med.* **2023**, *10*, 1083547. [CrossRef]
53. Zaromytidou, M.; Siasos, G.; Coskun, A.U.; Lucier, M.; Antoniadis, A.P.; Papafaklis, M.I.; Koskinas, K.C.; Andreou, I.; Feldman, C.L.; Stone, P.H. Intravascular hemodynamics and coronary artery disease: New insights and clinical implications. *Hell. J. Cardiol.* **2016**, *57*, 389–400. [CrossRef]
54. Candreva, A.; De Nisco, G.; Rizzini, M.L.; D'Ascenzo, F.; De Ferrari, G.M.; Gallo, D.; Morbiducci, U.; Chiastra, C. Current and future applications of computational fluid dynamics in coronary artery disease. *Rev. Cardiovasc. Med.* **2022**, *23*, 377. [CrossRef]
55. Barrere, N.; Brum, J.; L'her, A.; Sarasúa, G.L.; Cabeza, C. Vortex dynamics under pulsatile flow in axisymmetric constricted tubes. *Pap. Phys.* **2020**, *12*, 120002. [CrossRef]
56. Xu, L.; Chen, X.; Cui, M.; Ren, C.; Yu, H.; Gao, W.; Li, D.; Zhao, W. The improvement of the shear stress and oscillatory shear index of coronary arteries during Enhanced External Counterpulsation in patients with coronary heart disease. *PLoS ONE* **2020**, *15*, e0230144. [CrossRef] [PubMed]
57. Gijsen, F.; Katagiri, Y.; Barlis, P.; Bourantas, C.; Collet, C.; Coskun, U.; Daemen, J.; Dijkstra, J.; Edelman, E.; Evans, P.; et al. Expert recommendations on the assessment of wall shear stress in human coronary arteries: Existing methodologies, technical considerations, and clinical applications. *Eur. Heart J.* **2019**, *40*, 3421–3433. [CrossRef] [PubMed]
58. Secomb, T.W. Blood flow in the microcirculation. *Annu. Rev. Fluid Mech.* **2017**, *49*, 443–461. [CrossRef]
59. Grandchamp, X.; Coupier, G.; Srivastav, A.; Minetti, C.; Podgorski, T. Lift and down-gradient shear-induced diffusion in red blood cell suspensions. *Phys. Rev. Lett.* **2013**, *110*, 108101. [CrossRef] [PubMed]
60. Singh, R.K.; Li, X.; Sarkar, K. Lateral migration of a capsule in plane shear near a wall. *J. Fluid Mech.* **2014**, *739*, 421–443. [CrossRef]
61. Geislinger, T.M.; Franke, T. Hydrodynamic lift of vesicles and red blood cells in flow—From Fåhræus & Lindqvist to microfluidic cell sorting. *Adv. Colloid Interface Sci.* **2014**, *208*, 161–176. [CrossRef]
62. Franke, T.; Hoppe, R.H.W.; Linsenmann, C.; Schmid, L.; Willbold, C.; Wixforth, A. Numerical simulation of the motion of red blood cells and vesicles in microfluidic flows. *Comput. Vis. Sci.* **2011**, *14*, 167–180. [CrossRef]
63. Wu, W.T.; Yang, F.; Antaki, J.F.; Aubry, N.; Massoudi, M. Study of blood flow in several benchmark micro-channels using a two-fluid approach. *Int. J. Eng. Sci.* **2015**, *95*, 49–59. [CrossRef]
64. Starodumov, I.; Sokolov, S.; Blyakhman, F.; Zubarev, A.; Fedotov, S.; Alexandrov, D. In silico study of magnetic nanoparticles transport in channels of various diameters in the presence of a constant magnetic field. *Eur. Phys. J. Spec. Top.* **2023**, *232*, 1207–1217. [CrossRef]